

Nanobarcodes with multidimensional optical information beyond diffraction limit

Dayong Jin (✉ dayong.jin@uts.edu.au)

University of Technology Sydney <https://orcid.org/0000-0003-1046-2666>

Shihui Wen

University of Technology Sydney <https://orcid.org/0000-0002-4670-4658>

Yongtao Liu

University of Technology Sydney

Fan Wang

Institute for Biomedical Materials & Devices (IBMD), Faculty of Science, University of Technology Sydney, NSW 2007 <https://orcid.org/0000-0001-7403-3305>

Gungun Lin

Institute for Biomedical Materials and Devices (IBMD), Faculty of Science, University of Technology Sydney

jjajia zhou

University of Technology Sydney <https://orcid.org/0000-0002-0605-5745>

Bingyang Shi

Department of Biomedical Sciences, Faculty of Medicine & Health Sciences, Macquarie University

Yung Doug Suh

Korea Research Institute of Chemical Technology <https://orcid.org/0000-0003-2352-693X>

Article

Keywords: nanobarcodes, multidimensional optical information, diffraction limit, heterogeneous nanostructures

Posted Date: July 9th, 2020

DOI: <https://doi.org/10.21203/rs.3.rs-39284/v1>

License:  This work is licensed under a Creative Commons Attribution 4.0 International License.

[Read Full License](#)

Version of Record: A version of this preprint was published at Nature Communications on November 27th, 2020. See the published version at <https://doi.org/10.1038/s41467-020-19952-x>.

Abstract

Precise design and fabrication of heterogeneous nanostructures will enable nanoscale devices to integrate multiple desirable functionalities. But due to the diffraction limit (~ 200 nm), the optical uniformity and diversity within the heterogeneous functional nanostructures are hardly controlled and characterized. Here we report a set of nanobarcodes, each optically active section has its unique nonlinear responses to donut illumination patterns, so that one can discern each unit with super resolution. To achieve this, we first realized an approach of highly controlled epitaxial growth and produced a range of one-dimensional heterogeneous structures. Each section along the nanorod structure display tunable upconversion emissions, in four optically orthogonal dimensions, including colour, lifetime, excitation wavelength, and power dependency. Moreover, we demonstrated a 210 nm single nanorod as the smallest polychromatic light source for the on-demand generation of RGB photonic emissions. Remarkably, within a space of 50 nm, only 1/20th of the excitation wavelength, multiple codes can be successfully coded and decoded in 4 optical dimensions. This precision control enables the fabrication of super capacity geometrical barcodes with theoretical coding capacity up to $(24-1)^4$. This work benchmarks our new ability towards the full control of sub-diffraction-limit optical diversities of single heterogeneous nanoparticles.

Introduction

The frontier in nanomaterials engineering is to realize their composition control with atomic scale precision, so as to fabricate nanoscale structures with desirable morphological, interfacial and physical properties^{1,2}. The control in uniformity and tuning the diversities of single luminescent nanoparticles, dot to dot, has already enabled many quantitative measurements and high-performance nanophotonic devices^{3,4}. The next level of challenges and opportunities should be the controlled growth, manipulation and characterization of the hybrid and heterogeneous nanostructures that can incorporate multiple functionalities. But the nanoscale optical properties of such nanostructures are hardly accessible, due to the Abbe diffraction limit that confines the best axial and lateral resolutions of far field optical microscopy worse than 200 nm and 500 nm, respectively⁵.

Due to a wealth of electronic transitions within the 4f electron shells of lanthanide ions, nanostructures doped with lanthanide ions can form a unique class of functional optical devices^{6,7}. Among them, spherical upconversion nanoparticles (UCNPs) have been created with many unique optical properties, including tuneable colors⁸, multiplexed lifetimes^{9,10}, long-distance energy migration¹¹, amplified stimulated emissions¹²⁻¹⁶ and their responses to external fields of temperature¹⁷ and mechanical force¹⁸, which enables many novel applications, including full-colour displays⁸, solar energy harvesting¹⁹, security inks⁹, biomolecular sensing²⁰, force sensing²¹, nanothermometry^{22,23}, fluorescence microscopy¹², optical multiplexing²⁴, deep-tissue optogenetics²⁵, multimodal bio-imaging^{26,27} and light-triggered drug delivery^{28,29}.

Here we realize the artful control in the single-axis epitaxial growth of uniform one-dimensional lanthanide-doped nanoscale barcodes with high-dimensional optical signatures. Each section along the nanobarcode structure can be controlled to display tunable emissions and decoded by the super-resolution microscopy, in four optically orthogonal dimensions. Within a space of 50 nm, multiple codes are successfully coded and decoded in four optical dimensions. This precision control has enabled the fabrication of super capacity geometrical barcodes with theoretical coding capacity up to $(2^4-1)^4$.

Results

Single-axis growth of heterogeneous nanobarcodes

Fig. 1a summarizes the key procedure and critical conditions that lead to the desirable integration of photonics functionalities. The principle that directs the controlled epitaxial growth is based on the fact that the surfactants - oleic acid molecules (OAH) prefer to attach on the (001) facet while the oleic acid anions (OA^-) bind more firmly onto the (100)/(010) facets of a $\beta\text{-NaYF}_4$ nanocrystal³⁰. Here we find that at a high OA^-/OAH ratio (1:2) and slightly increased reaction temperature (310 °C), the crystal growth rate on the (001) facet can be a lot faster than that on the (100)/(010) facets and heterogeneous nanorods can be formed. For controlled one-axis nanocrystals formation, the amount of the precursor should be kept sufficiently low for the directional growth process. For instance, when the concentration of the NaYF_4 shell precursor is kept at relatively high level (0.732 mmol/mL), the growth rates of 1.68 atomic layers per min on the (001) facet versus 0.26 atomic layer per min on the (100)/(010) facets were observed (Supplementary Text). If the supply of precursors is less than the demands in the epitaxial growth from the two (001) facets of the core nanocrystals (0.235 mmol/mL), desirable single-axis growth could be achieved (Fig. S1 - S3). Notably, in the heterogeneous epitaxial growth process of nanorods, high OA^- concentration is critical to avoid the formation of the dumbbell and core@shell structures of NaNdF_4 and NaLnF_4 (Ln = Yb, Er, Tm), respectively (Fig. S4 and S5).

Morphology uniformity of heterogeneous nanobarcodes

By achieving such a strict control, the HAADF-STEM micrographs (Fig. 1b) show the fabrication of a series of heterogeneous rod structures with each segment of tunable length (e.g. 5 nm and 10 nm) by adjusting the time for precursor injection. Also, the number of the segments can be well controlled (e.g. 10 and 18 segments) by controlling the composition of precursors. Figure 1c shows a large area HAADF-STEM image of highly uniform 18-segment nanorod structures with a consistent length of 5 nm for each segment. The invariant 42 nm of the diameter for the heterogeneous rods with different segments confirms the absolute control in the single-axis growth (Fig. S6). Remarkably, the statistical results shown in Fig. 1d further confirm that these nanorods are exceptionally uniform even in the thickness of each segment. By calculating the precursor injection speed and the thickness of each segment, it is shown that the growth rates of both NaYF_4 and NaErF_4 on the (001) facet are one atomic layer per min. The use of the inert segments of NaYF_4 in the one-dimensional heterogeneous nanorods can minimize the

diffusions of optically active ions and therefore allow arbitrary integration of multiple and orthogonal optical responses to form nanobarcodes.

Super resolving nanobarcodes' optical segments

To super resolve the optical information of different segments of single nanobarcodes, we employ an annular excitation profile (donut-shape illumination beam) in a typical confocal microscopy setup. As illustrated in Fig. 2a, the size of the donut beam is large with a full-width at half-maximum (FWHM) around 300 nm, set by the diffraction limit of the excitation point spread function (PSF). By taking advantage of both the non-linear optical responses of upconversion luminescence and its low saturation intensity levels, the emission PSF can produce a much smaller dark area, with the FWHM down to around 29 nm (Fig. S7b-c), allowing the emission saturation mode to be used for super-resolution imaging.³¹ Note that instead of the stimulated emission depletion (STED) super-resolution microscopy configuration^{12-14,32} that only works for depleting the emissions from UCNPs doped with Tm^{3+} ions, our current method is a lot simpler and broadly compatible with different emitters, doping concentrations, and emission bands.³¹ The use of a single beam donut illumination design avoids the sophisticated system alignment and temporal synchronization of both Gaussian excitation and donut depletion beams required by STED.

We first decode a set of sub-diffraction-limit nanobarcodes with a pair of the identical active segments grown on both ends. As shown in Fig. 2b, by a donut-shaped excitation beam scan across heterogeneous nanorods, a negative contrast will be generated when any one of the optically active units is positioned within the donut beam, so that the final image of a single nanobarcode will be presented as two negative-contrast spots (1 and 3), as shown in Fig. 2c. As the spatial resolution of our emission saturation mode microscopy is 29 nm (Fig. S7 b-c), the limit in decoding the two active segments is at the distance of 50 nm (see our simulation results in Fig. S7d-f). To experimentally verify the optical resolving power, we further fabricate five batches of distance-tuneable nanobarcodes (Fig. S8). As the centroids of the dark spots in each negative super-resolution image (Fig. 2d and Fig. S9) can be used to localize the active segments in the nanobarcodes, the super-resolution images of the five types of representative nanobarcodes shows the central distance increasing from 76 to 141 nm, which is highly consistent with the TEM results (Fig. 2e). As the length of the active segments is around 20 nm, the separation distance between active units (the length of the inert section) is 55 to 120 nm (Fig. S8). These results confirm the spatial decoding power of our single-beam super resolution approach as around 55 nm, which is comparable to the reported super-resolution techniques used for barcode decoding.³³⁻³⁶ Notably, due to the nonlinear power dependence property of the emission PSF, choosing an appropriate excitation power is critical in optimizing the localization accuracy (Fig. S10).

Moreover, as shown in Fig. 2f and Fig. S11a, the single-donut-beam approach can be used to resolve the high-density nanobarcodes. By taking advantage of the pair of identical segments on each single nanorod, the sample distance of as close as 69.8 nm, significantly below the diffraction limit, can be super resolved. Furthermore, as shown Fig. 2g and Fig. S11b, the super-resolution approach can

successfully resolve two populations of nanobarcodes with active segmental distances of 90 nm and 120 nm, respectively. The distance between two types of nanobarcodes as close as 59.2 nm has been resolved. These results highlight the advantage of our geometrical barcode with structural rigidity compared to other soft barcodes.^{34,37}

Selective activation of nanobarcodes' segments

The optically active units doped by lanthanide ions, typically with characteristic 'ladder-like' multiple excited states, can generate near infrared (NIR), visible, and ultraviolet luminescence with sharp spectrum, large (anti-)Stokes shift, and inherent long lifetime.^{11,38-40} As the emission saturation super resolution mode is not limited by the types of lanthanide emitters, we can code and decode the nanorods by using a diverse choice of lanthanide co-dopants. First, it is rather a straight-forward strategy by collecting the emission information from different wavelength windows, i.e., NIR and red emissions from Tm^{3+} and Er^{3+} emitters (Fig. S12), respectively. Then, we also evaluate the new capability using different concentrations of emitters in each segment. The power-dependent property^{38,41} (Fig. 3a) allows the selective activating the segments of nanobarcodes beyond the diffraction limit. Selective activation of two sections doped by the relatively lower concentration of emitters (4% Tm^{3+}) and higher concentration of emitters (10% Tm^{3+}) can be achieved by using low and high power density of 980 nm excitation, respectively (Fig. 3b). The distances of different active pairwise are consistent with that from the TEM characterization (Fig. 3c-d and Fig. S13). Notably, the emission difference from the two segments can be further decoded by the time-resolved mode, as the highly doped sections display a much shorter lifetime (Fig. S14).

Visualizing interfacial energy transfer within nanobarcode

We can further decode the information encoded through interfacial energy transfer and migration in heterogeneous upconversion system. Here, by designing the $\text{Yb}^{3+}/\text{Er}^{3+}$ co-doped upconversion segment closely packed with $\text{Yb}^{3+}/\text{Nd}^{3+}$ co-doped sensitization segments (Fig. 3e), we show the selective activation and decoding of these neighbouring segments. This is achieved by either exciting the upconversion segment using the 980 nm donut illumination or the nearby sensitization segments by the 808 nm donut illumination, where the energy migration from $\text{Nd}^{3+} \rightarrow \text{Yb}^{3+} \rightarrow \text{Yb}^{3+} \rightarrow \text{Er}^{3+}$ occur across the interface. Because the 808 nm donut excitation only examines where the material absorbs, we can localize the photon-sensitization segments with Nd^{3+} as dopants (Fig. S15). Following the same principle, the 980 nm donut excitation is responsible for diagnosing the location of Yb^{3+} ions by reading the Er^{3+} emissions. The super-resolution images (Fig. 3f) clearly reveals both the Nd^{3+} and Yb^{3+} sensitization segments with the centre-to-centre distance around 7.2 nm, which is further verified by the TEM characterization (Fig. 3g, 3 h and Fig. S15). For the first time, we precisely localize the position of closely packed sensitizer sections and visualize the energy transfer effect at nanoscale. The developed method have the potential to precisely study the interfacial energy transfer across two neighbouring segments, which will further open the door for fine tuning of the emission¹¹ and excitation⁴² wavelengths, emission intensity⁴³ and lifetimes¹⁷.

Sub-diffraction-limit RGB-switchable pixel

The ability of selective activations of high-dimensional emission diversities from a single nanorod can further create a sub-diffraction-limit RGB-switchable pixel, on demand and in response to the specific excitation wavelength and illumination pattern, as illustrated in Fig. 4. This experiment takes advantage that the tunable donut and Gaussian excitation profiles at 980 nm and 808 nm can be commensurate to the bilateral symmetry of the barcode stratification. When a relatively large 980 nm donut excitation is used, only the pair of Red units ($\text{NaYF}_4:30\%\text{Yb}^{3+},2\%\text{Er}^{3+}$) on the end of the rod can be selectively illuminated. The smaller size of 980 nm donut excitation only activates the pair of Blue units ($\text{NaYF}_4:40\%\text{Yb}^{3+},4\%\text{Tm}^{3+}$) in the middle of the nanorods. And the 808 nm confocal spot of excitation is responsible for illuminating the central Green emission unit ($\text{NaYF}_4:15\%\text{Er}^{3+}$), since neither of the Red unit or the Blue unit has the effective absorbance at 808 nm. White emission can be generated through the combined use of the 808 nm confocal and 980 donut excitations. These results show our ability to selectively activate different optical units in heterogeneous nanostructures, which opens the door to build more sophisticated nanophotonic devices that can on-demand display a set of high-dimensional digitized photonic emissions with super-capacity optical information storage.

Super-capacity optically orthogonal nanobarcodes

Using the controlled single-axis epitaxial growth approach and the donut-shaped illumination, we develop a four-dimensional (4D) optical barcoding technique within the diffraction limit. The four orthogonal dimensions include excitation wavelength, power density, emission wavelength and emission lifetime (Fig. 5a). The combination allows us to arbitrarily assemble the many multiple functional segments with the diverse optical properties within a heterogeneous nanorod. Figure 5b shows one batch of such a highly uniform nanoscale barcode structure with six distinct segments, separated by a ~ 2.5 nm inert NaYF_4 layer. Donut-shaped illumination leads to the super-resolution decoding of the sophisticated optical signatures in the four channels of optical dimensions (Fig. S17-18). Figure 5c shows a typical super-resolution image of the optical barcodes in 4D, which is in stark contrast with the conventional confocal images. Notably, the pairwise design of the segments allows false alarm rate-free decoding for the multi-dimensional super-capacity optical barcodes. Within a space of 50 nm, only 1/20th of the excitation wavelength, we demonstrate the precision control in coding and decoding of four codes (Fig. 5c), which has higher coding density than any geometrical barcodes reported in literatures^{34,36,44,45}. Through freely adjusting the distance and the order of different codes, this precision control has enabled the fabrication of super capacity geometrical barcodes that can potentially produce up to $(2^4-1)^4$ digits of optical nanobarcodes. As a demonstration, we summarize additional part of this barcode library in the supporting information Figure S19. To our knowledge, this represents the smallest geometrical barcode with super-capacity optical multiplexing capability to encode large amounts of information^{33,34,36}.

Discussion

We demonstrated here an important advance in coding and decoding of optical information at the nanoscale and many potentials in utilising the sub-diffraction-limit optical characterization and selective activation of doping units with a set of high-dimensional digitized and differentiable photonic emissions. Both the artful growth of a library of heterogeneous nanostructures with exceptionally high uniformity and precise discerning of diverse non-linear responses at super-resolution are the key technology enablers. We anticipate that such barcode structures would attract broad interests in a range of applications as information nanocarriers for bio-nanotechnology, life sciences, data safety and storage, once they are incorporated into a variety of matrixes.^{35,36,46} The inorganic nanobarcode structures are rigid and it is easy to control the distance accuracy of different codes for the geometrical encoding, in stark contrast with soft geometric barcode counterparts such as dye-tagged DNA barcodes.^{34,37} Moreover, they are chemically and optically stable, which enables them as idea information-coded nanocarriers for drug delivery and long time tracking, once the surface of the barcode structures is further modified and functionalized with probe molecules and cargos.^{7,29} The developed geometrical nanobarcodes could be simultaneously used for tagging different cellular species and identified by the super-resolution nanoscopy, bypassing the need for the stepwise addition of dyes for multiplexed imaging of intracellular structures.^{47,48} The speed of this super-resolution technique remains low, but this disadvantage can also be circumvented by employing parallelized scanning with beam arrays in the future.⁴⁹ These nanobarcodes are also readily applicable for high-security anticounterfeiting when different batches of them are blended with inks and can be readily printed on high-value products for authentication.³⁵ Not limiting to technological applications, the geometrically distinct nanostructures provides a unique model for photophysics study, including the dynamics of one-dimensional energy transfer and have the potential to open the door for optical study of heterogeneous nanomaterials.

Methods

Details and any associated references are provided in the Supplementary Information.

Declarations

Data availability

All the relevant data are available from the correspondence authors upon reasonable request.

References

1. Zhou, J., Chizhik, A. I., Chu, S. & Jin, D. Single-particle spectroscopy for functional nanomaterials. *Nature* **579**, 41–50 (2020).
2. Steimle, B. C., Fenton, J. L. & Schaak, R. E. Rational construction of a scalable heterostructured nanorod megalibrary. *Science* **367**, 418–424 (2020).
3. Yan, R., Gargas, D. & Yang, P. Nanowire photonics. *Nat. Photon.* **3**, 569 (2009).

4. Ozbay, E. Plasmonics: Merging Photonics and Electronics at Nanoscale Dimensions. *Science* **311**, 189–193 (2006).
5. Jin, D. *et al.* Nanoparticles for super-resolution microscopy and single-molecule tracking. *Nat. Methods* **15**, 415–423 (2018).
6. Qin, X., Liu, X., Huang, W., Bettinelli, M. & Liu, X. Lanthanide-Activated Phosphors Based on 4f-5d Optical Transitions: Theoretical and Experimental Aspects. *Chem. Rev.* **117**, 4488–4527 (2017).
7. Auzel, F. Upconversion and Anti-Stokes Processes with f and d Ions in Solids. *Chem. Rev.* **104**, 139–174 (2004).
8. Deng, R. *et al.* Temporal full-colour tuning through non-steady-state upconversion. *Nat. Nanotech.* **10**, 237–242 (2015).
9. Lu, Y. *et al.* Tunable lifetime multiplexing using luminescent nanocrystals. *Nat. Photon.* **8**, 32–36 (2014).
10. Fan, Y. *et al.* Lifetime-engineered NIR-II nanoparticles unlock multiplexed in vivo imaging. *Nat. Nanotech.* **13**, 941–946 (2018).
11. Wang, F. *et al.* Tuning upconversion through energy migration in core–shell nanoparticles. *Nat. Mater.* **10**, 968–973 (2011).
12. Liu, Y. *et al.* Amplified stimulated emission in upconversion nanoparticles for super-resolution nanoscopy. *Nature* **543**, 229–233 (2017).
13. Zhan, Q. *et al.* Achieving high-efficiency emission depletion nanoscopy by employing cross relaxation in upconversion nanoparticles. *Nature Communications* **8**, 1058 (2017).
14. Bednarkiewicz, A., Chan, E. M., Kotulska, A., Marciniak, L. & Prorok, K. Photon avalanche in lanthanide doped nanoparticles for biomedical applications: super-resolution imaging. *Nanoscale Horizons* **4**, 881–889 (2019).
15. Fernandez-Bravo, A. *et al.* Continuous-wave upconverting nanoparticle microlasers. *Nature Nanotechnology* **13**, 572–577 (2018).
16. Fernandez-Bravo, A. *et al.* Ultralow-threshold, continuous-wave upconverting lasing from subwavelength plasmons. *Nature Materials* **18**, 1172–1176 (2019).
17. Zhou, J. *et al.* Activation of the surface dark-layer to enhance upconversion in a thermal field. *Nature Photonics* **12**, 154–158 (2018).
18. Lay, A. *et al.* Bright, Mechanosensitive Upconversion with Cubic-Phase Heteroepitaxial Core–Shell Nanoparticles. *Nano Letters* **18**, 4454–4459 (2018).
19. Hao, S. *et al.* Enhancing dye-sensitized solar cell efficiency through broadband near-infrared upconverting nanoparticles. *Nanoscale* **9**, 6711–6715 (2017).
20. Su, Q., Feng, W., Yang, D. & Li, F. Resonance Energy Transfer in Upconversion Nanoplatfoms for Selective Biodetection. *Acc. Chem. Res.* **50**, 32–40 (2017).
21. Lay, A. *et al.* Optically Robust and Biocompatible Mechanosensitive Upconverting Nanoparticles. *ACS Central Science* **5**, 1211–1222 (2019).

22. Ximendes, E. C. *et al.* Unveiling in Vivo Subcutaneous Thermal Dynamics by Infrared Luminescent Nanothermometers. *Nano Letters* **16**, 1695–1703 (2016).
23. Qiu, X. *et al.* Ratiometric upconversion nanothermometry with dual emission at the same wavelength decoded via a time-resolved technique. *Nature Communications* **11**, 4 (2020).
24. Zhou, L. *et al.* Single-band upconversion nanoprobe for multiplexed simultaneous in situ molecular mapping of cancer biomarkers. *Nat. Commun.* **6**, 6938 (2015).
25. Chen, S. *et al.* Near-infrared deep brain stimulation via upconversion nanoparticle-mediated optogenetics. *Science* **359**, 679–684 (2018).
26. Cheng, L. *et al.* Facile Preparation of Multifunctional Upconversion Nanoprobes for Multimodal Imaging and Dual-Targeted Photothermal Therapy. *Angew. Chem. Int. Ed.* **50**, 7385–7390 (2011).
27. Ni, D. *et al.* Single Ho³⁺-Doped Upconversion Nanoparticles for High-Performance T₂-Weighted Brain Tumor Diagnosis and MR/UCL/CT Multimodal Imaging. *Adv. Funct. Mater.* **24**, 6613–6620 (2014).
28. min, Y., Li, J., Liu, F., Yeow, E. K. L. & Xing, B. Near-Infrared Light-Mediated Photoactivation of a Platinum Antitumor Prodrug and Simultaneous Cellular Apoptosis Imaging by Upconversion-Luminescent Nanoparticles. *Angew. Chem.* **126**, 1030–1034 (2014).
29. Yang, D. *et al.* Current advances in lanthanide ion (Ln³⁺)-based upconversion nanomaterials for drug delivery. *Chem. Soc. Rev.* **44**, 1416–1448 (2015).
30. Liu, D. *et al.* Three-dimensional controlled growth of monodisperse sub-50 nm heterogeneous nanocrystals. *Nat. Commun.* **7**, 10254 (2016).
31. Chen, C. *et al.* Multi-photon near-infrared emission saturation nanoscopy using upconversion nanoparticles. *Nature Communications* **9**, 3290 (2018).
32. Shin, K. *et al.* Distinct mechanisms for the upconversion of NaYF₄:Yb³⁺,Er³⁺ + nanoparticles revealed by stimulated emission depletion. *Physical Chemistry Chemical Physics* **19**, 9739–9744 (2017).
33. Oracz, J. *et al.* Ground State Depletion Nanoscopy Resolves Semiconductor Nanowire Barcode Segments at Room Temperature. *Nano Letters* **17**, 2652–2659 (2017).
34. Lin, C. *et al.* Submicrometre geometrically encoded fluorescent barcodes self-assembled from DNA. *Nature Chemistry* **4**, 832 (2012).
35. Shikha, S., Salafi, T., Cheng, J. & Zhang, Y. Versatile design and synthesis of nano-barcodes. *Chemical Society Reviews* **46**, 7054–7093 (2017).
36. Lin, G., Baker, M. A. B., Hong, M. & Jin, D. The Quest for Optical Multiplexing in Bio-discoveries. *Chem* **4**, 997–1021 (2018).
37. Schmied, J. J. *et al.* DNA origami-based standards for quantitative fluorescence microscopy. *Nature Protocols* **9**, 1367–1391 (2014).
38. Gargas, D. J. *et al.* Engineering bright sub-10-nm upconverting nanocrystals for single-molecule imaging. *Nat. Nanotech.* **9**, 300–305 (2014).
39. Nam, S. H. *et al.* Long-Term Real-Time Tracking of Lanthanide Ion Doped Upconverting Nanoparticles in Living Cells. *Angewandte Chemie International Edition* **50**, 6093–6097 (2011).

40. Chan, E. M. Combinatorial approaches for developing upconverting nanomaterials: high-throughput screening, modeling, and applications. *Chemical Society Reviews* **44**, 1653–1679 (2015).
41. Wang, F. *et al.* Microscopic inspection and tracking of single upconversion nanoparticles in living cells. *Light Sci. Appl.* **7**, e18007 (2018).
42. Wang, Y.-F. *et al.* Nd³⁺-Sensitized Upconversion Nanophosphors: Efficient In Vivo Bioimaging Probes with Minimized Heating Effect. *ACS Nano* **7**, 7200–7206 (2013).
43. Zhong, Y., Rostami, I., Wang, Z., Dai, H. & Hu, Z. Energy Migration Engineering of Bright Rare-Earth Upconversion Nanoparticles for Excitation by Light-Emitting Diodes. *Adv. Mater.* **27**, 6418–6422 (2015).
44. Zhang, Y. *et al.* Multicolor Barcoding in a Single Upconversion Crystal. *Journal of the American Chemical Society* **136**, 4893–4896 (2014).
45. Lee, J. *et al.* Universal process-inert encoding architecture for polymer microparticles. *Nature Materials* **13**, 524 (2014).
46. Xu, Y., Wang, H., Chen, B., Liu, H. & Zhao, Y. Emerging barcode particles for multiplex bioassays. *Science China Materials* (2018).
47. Beliveau, B. J. *et al.* Single-molecule super-resolution imaging of chromosomes and in situ haplotype visualization using Oligopaint FISH probes. *Nature Communications* **6**, 7147 (2015).
48. Kishi, J. Y. *et al.* SABER amplifies FISH: enhanced multiplexed imaging of RNA and DNA in cells and tissues. *Nature Methods* **16**, 533–544 (2019).
49. Chmyrov, A. *et al.* Nanoscopy with more than 100,000 'doughnuts'. *Nature Methods* **10**, 737–740 (2013).

Figures

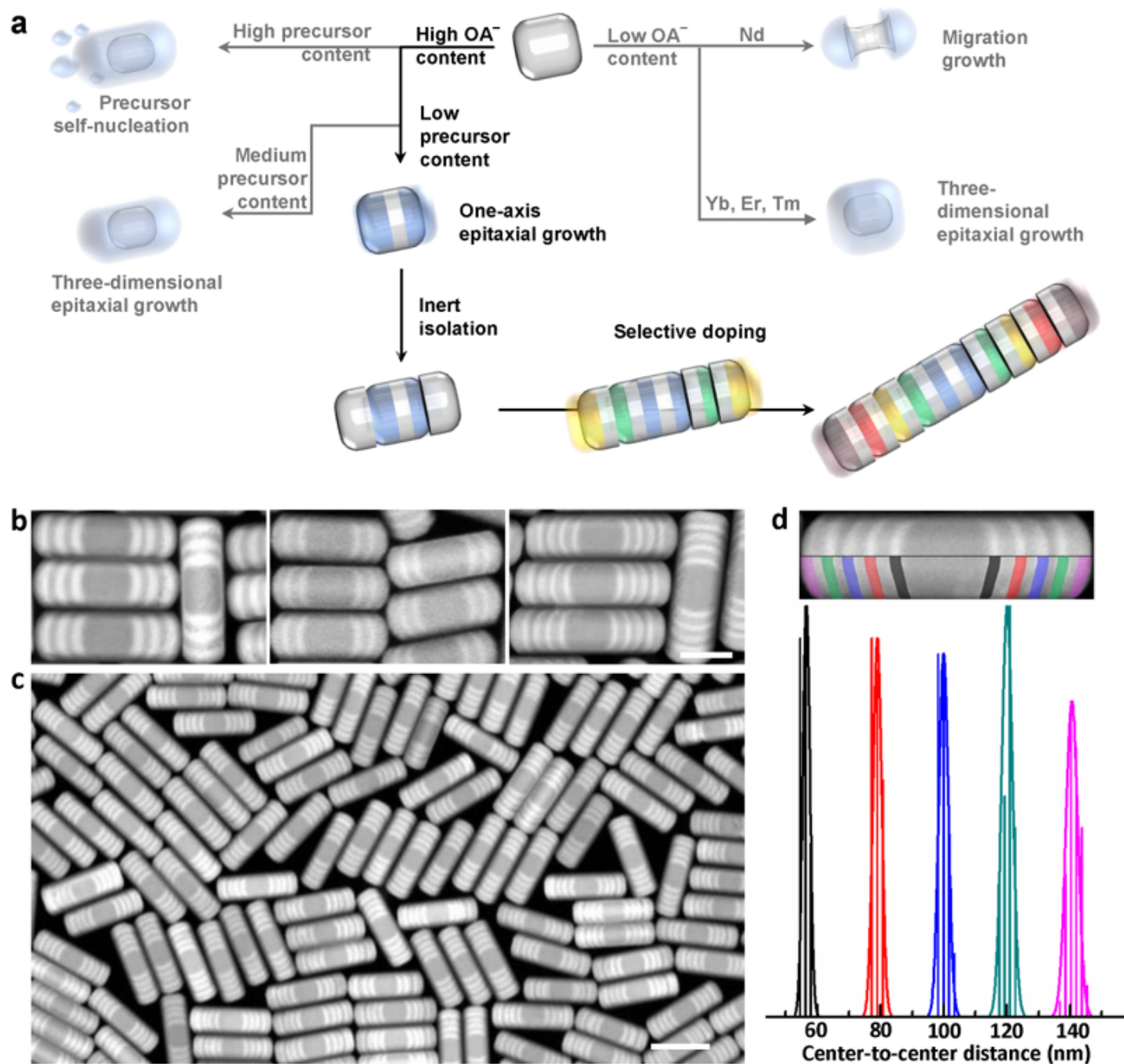


Figure 1

Single-axis epitaxial controlled growth of heterogeneous nanoscale barcodes. (a) Schematic diagram to illustrate the route that leads to the formation of the one-dimensional nanorods. Conditions, including the well-controlled amount of surfactant concentration (OA⁻) and the relatively low concentration of shell precursor, have to be met, otherwise, nanoplates, nanodumbbells, nanoparticles of inhomogeneous phases, and small nanoparticles from precursor self-nucleation, will form. (b) High-angle annular dark-field scanning transmission electron microscopy (HAADF-STEM) images of three typical heterogeneous nanorods, including 10-segment NaYF₄-NaErF₄(10nm)-NaYF₄(5nm)-NaErF₄(10nm)-NaYF₄(5nm)-NaErF₄(10nm), 10-segment NaYF₄-NaErF₄(5nm)-NaYF₄(5nm)-NaErF₄(5nm)-NaYF₄(5nm)-NaErF₄(5nm),

and 18-segment NaYF₄-NaErF₄(5nm)-NaYF₄(5nm)-NaErF₄(5nm)-NaYF₄(5nm)-NaErF₄(5nm)-NaYF₄(5nm)-NaErF₄(5nm)-NaYF₄(5nm)-NaErF₄(5nm) nanorods, scale bar is 50 nm. (c) Large area HAADF-STEM image of 18-segment heterogeneous nanorods, scale bar is 100 nm. (d) Distance statistics of five pairwise NaErF₄ segments (centre-to-centre of each pairwise with different colour markers) of the heterogeneous nanorods in c.

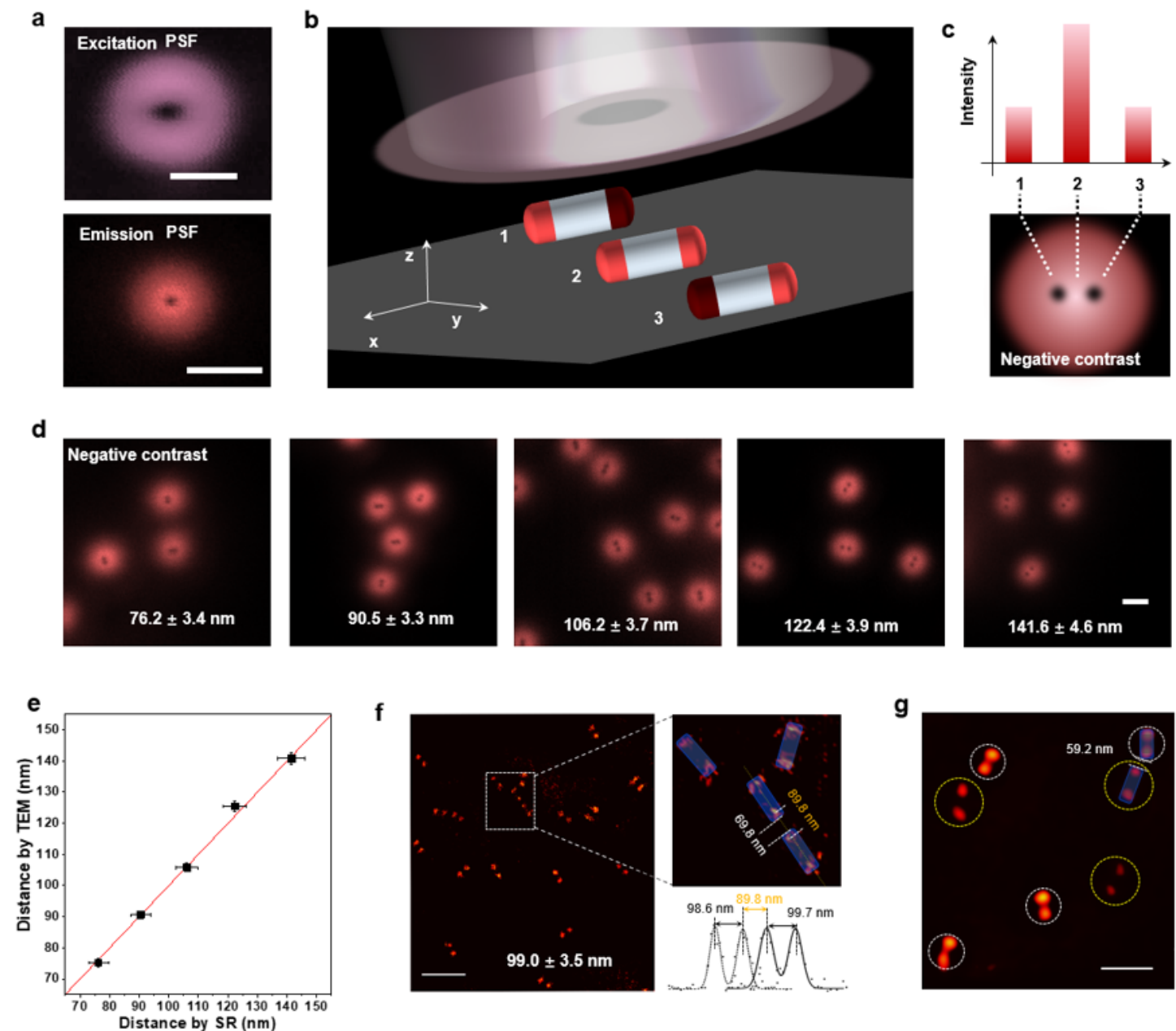


Figure 2

Super-resolution decoding optical nanobarcodes with different length. (a) The pattern of the donut-shaped illumination of excitation point spread function (PSF) and the pattern of the resulted emission PSF after scanning across a single UCNPs. (b) Illustration of a process using a donut-shaped excitation beam to scan and resolve the heterogeneous structure of single upconversion nanorod. (c) The corresponding luminescence intensities at the three typical positions to resolve the final super-resolution

negative-contrast image of a nanorod. (d) The raw data of negative-contrast super-resolution images of five types of heterogeneous upconversion nanorods with tuneable lengths between the optically active components images. (e) The average center-to-center distance and standard deviation of two actively doped segments of five types of heterogeneous upconversion nanobarcodes measured from TEM and super-resolution imaging. (f) Super-resolution image of the high concentration nanobarcodes with active segmental distances of 99.0 nm. (g) Super-resolution image of the mixture of two types of nanobarcodes with active segmental distances of 90 nm and 122 nm, respectively. Pixel sizes in d, g, and h are 10 nm. Scale bars in a, d, f, and g are 500, 500, 400, and 250 nm, respectively.

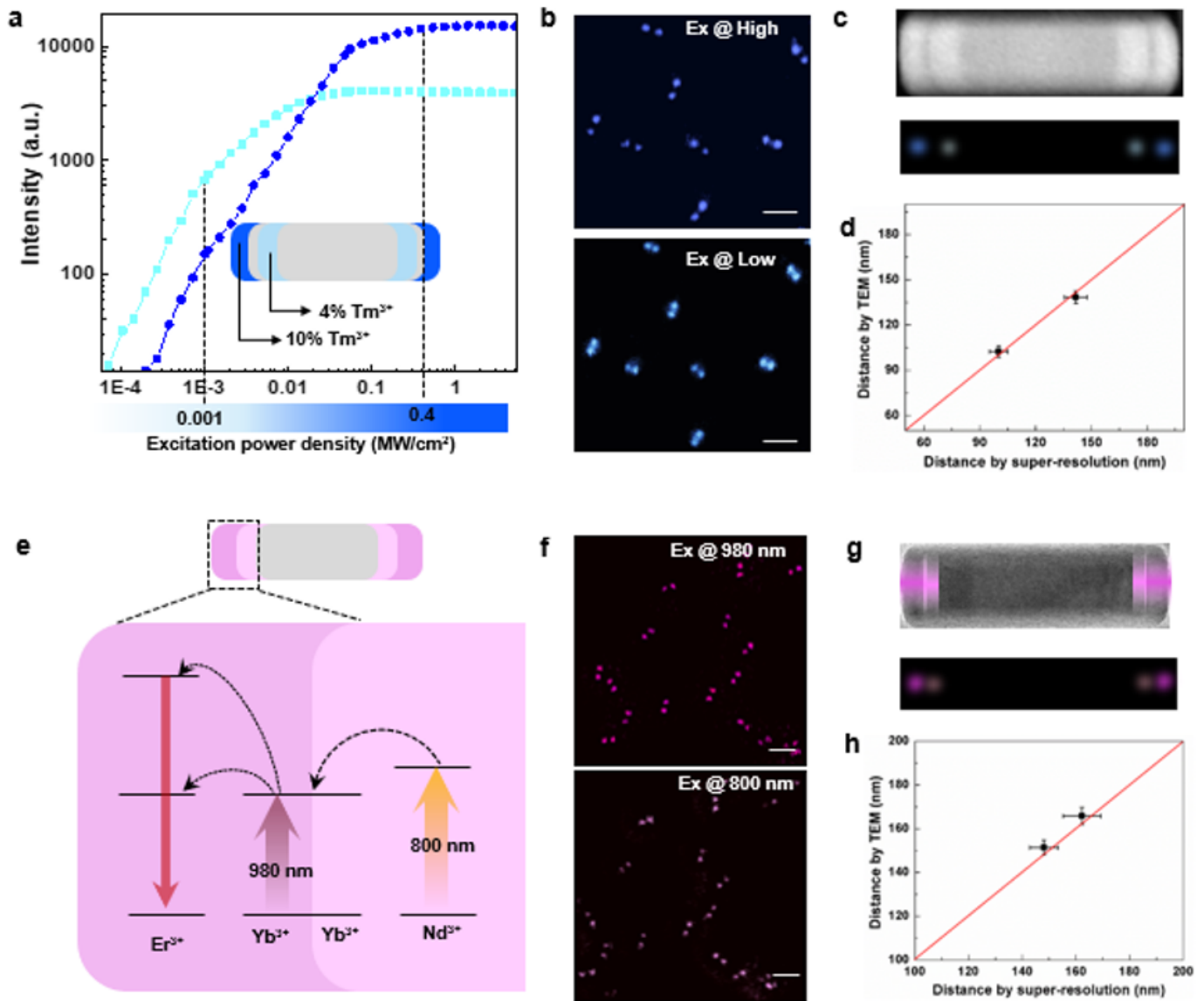


Figure 3

Super-resolution decoding nanobarcodes with different optical dimensions. (a) The scheme using the excitation-power-dependent property to activate the different segments of a purpose-designed nanobarcode. The upconversion emissions, generated from the segment doped with relatively higher concentration (10% Tm³⁺), can be turned on at higher excitation power density, compared with that from

lower doped (4% Tm³⁺) segments. (b) Super-resolution images of the functional segments selectively decoded by high and low power density conditions. (c) HAADF-STEM image and corresponding two-channel super-resolution image. (d) Statistical analysis of the distance distributions of different sections measured by TEM images and super-resolution images. (e) The scheme using the long-distance energy migration property to activate the nearby segments for decoding the location of different sensitizers. (f) Super-resolution images of the functional segments selectively decoded by 980 nm and 808 nm excitation. (g) TEM image and corresponding two excitation-wavelength-channel super-resolution image. (h) Statistical analysis of the distance distributions of different sections measured by TEM images and super-resolution images. Pixel sizes in b and f are 10 nm. Scale bars are 200 nm. High-resolution images of b and f are shown in Supporting information Fig S16.

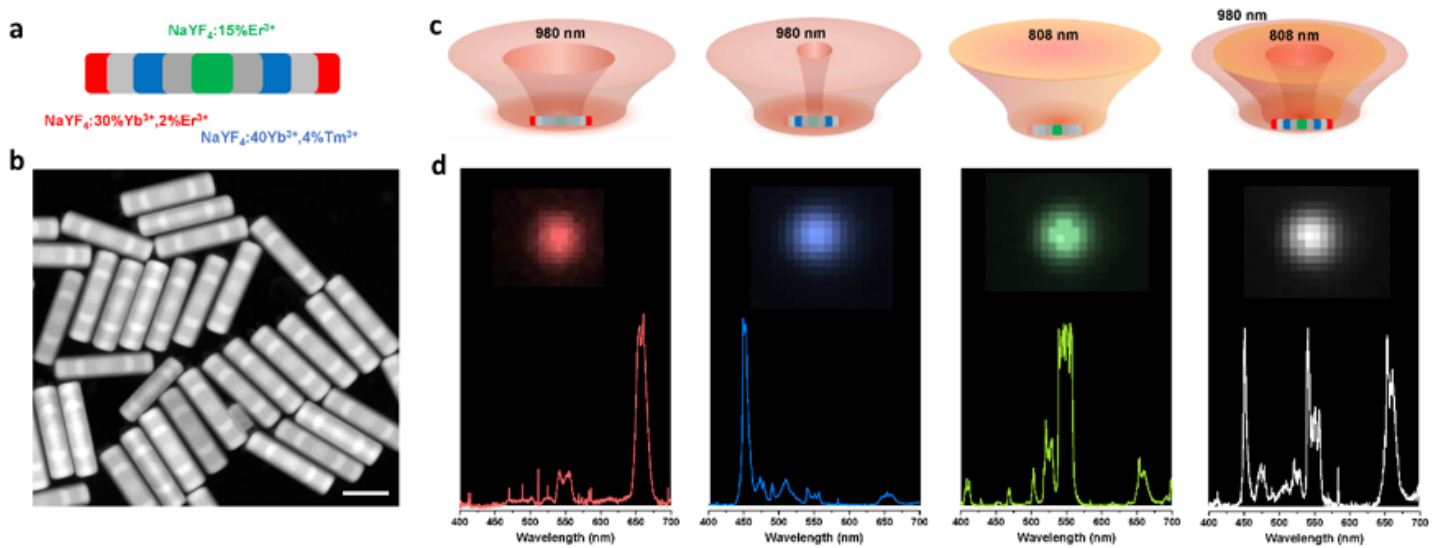


Figure 4

On-demand generation of RGB colours from a single nanobarcode. (a) The scheme to integrate multiple segments with different dopants, each responsible for emitting red, blue, and green colours. (b) HAADF-STEM image of the heterogeneous 210 nm optical barcodes, scale bar is 100 nm. (c) Diagrams of the bright upconversion emissions with switchable colours in response to the illumination patterns of a Gauss-Laguerre mode donut profile (980 nm) and a Gaussian excitation profile (808 nm). (d) Wide-field microscopy images of a single barcode and their corresponding luminescence spectra under the different illumination conditions in c.

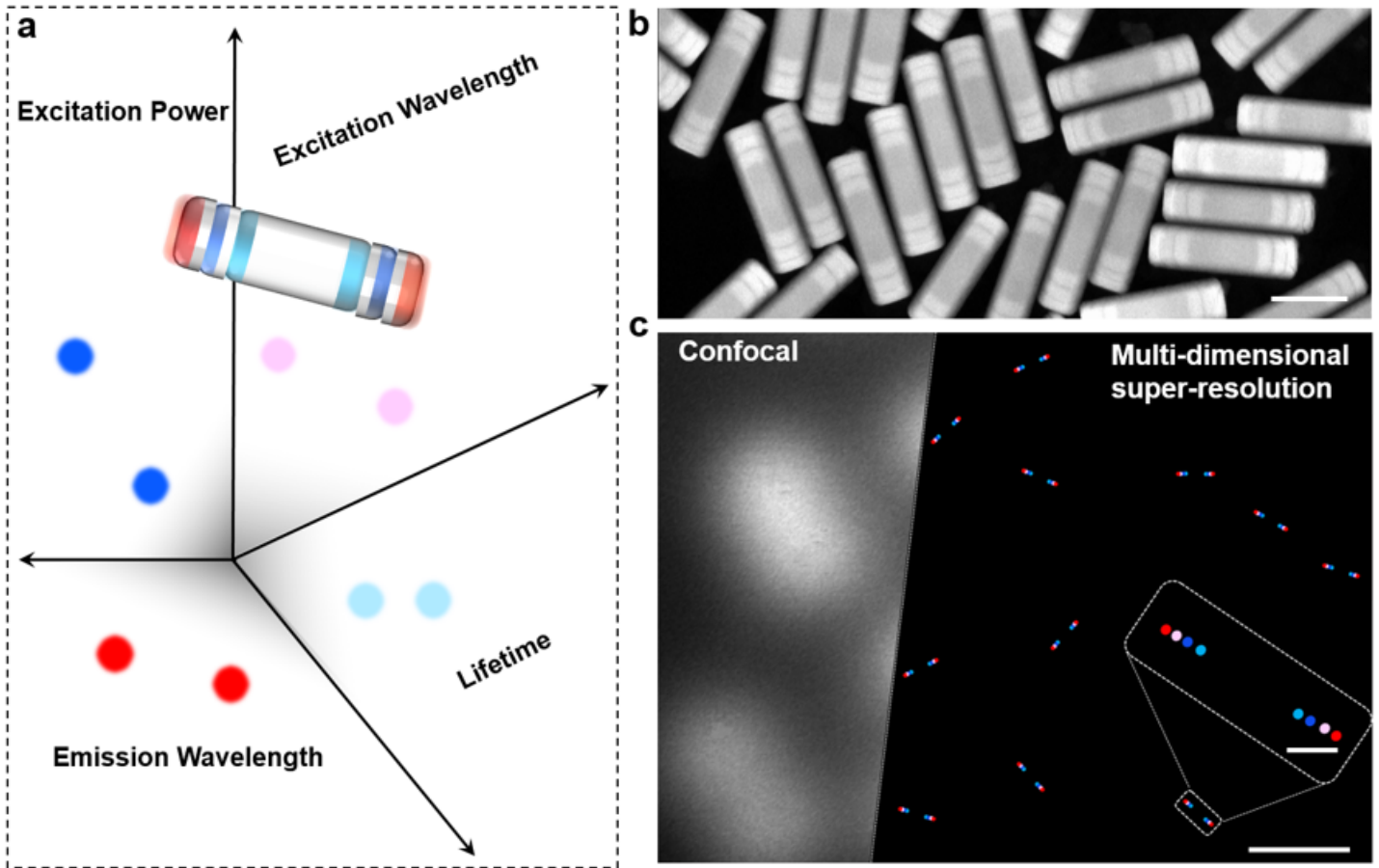


Figure 5

Super-capacity four-dimensional optical nanobarcode. (a) The scheme to integrate multiple sub-20nm segments into one nanobarcode, each segment contains optical codes from one orthogonal optical dimension, four pseudocolor was used to represent optical codes from four orthogonal optical dimensions (including Excitation power (blue), excitation wavelength (pink), emission wavelength (red), and lifetime (light blue)). (b) HAADF-STEM image of the heterogeneous nanoscale optical barcodes, scale bar is 100 nm. (c) Confocal (diffraction-limited image) and multi-dimensional super-resolution images of the nanobarcode, scale bar is 500 nm. Inset shows an enlarged super-resolution barcode containing multi-dimensional optical information, scale bar is 50 nm.

Supplementary Files

This is a list of supplementary files associated with this preprint. Click to download.

- [SI1July.docx](#)